Folded strains of a bistable composite tape-spring

Bing Wang[1,2*], Keith A Seffen[2], Simon D Guest[2]

[1] School of Mechanical Engineering & Automation, Fuzhou University, Fuzhou, 350108, China
[2] Department of Engineering, University of Cambridge, Cambridge, CB2 1PZ, UK
Corresponding to: b.wang@fzu.edu.cn

Abstract: The bistable composite tape-spring (CTS) structure has received increasing interest in industrial applications, especially in aerospace engineering. Its ability to fold under large displacements makes it attractive as a hinge-safety assembly, with reduced weight, complexity and maintenance compared to the conventional lock-link connections. The shape of a CTS during folding has been studied; but research on its folded strain levels is limited. We devise a novel method to evaluate the strain evolution in a folded CTS. This is achieved by embedding strain gauges in a CTS sample before ‘‘rolling’’ the fold through them at constant fold angle: the rolling shape thus provides an exact profile of the strain along the CTS centreline. The strain has maximum levels at the centre of the folded CTS, as expected, whilst a new shoulder-like local peak feature is observed. A finite element (FE) analysis is performed to reveal expected levels of strain: the experimental strain profile is then compared to reveal fundamental correlations. Further insight therefore can be drawn from the FE model, which is beneficial in maintaining structural integrity, and ensure the composite is not over-confined and liable to damage during and after folding.

Keywords: Composite; tape-spring; structural; strain; finite element analysis.

1 Introduction

A bistable composite tape-spring (CTS) is a thin-shell open slit tube with fibres oriented at ±45°. It is stable in both the extended and coiled states, and can endure large deformation during folding. It is proposed for use in aircraft landing gear systems to replace the conventional lock-link hinge assemblies (Schmidt, 2017). Previous studies on the CTS have mainly focused on the mechanism of its bistability (Galletly and Guest, 2004a, 2004b; Guest and Pellegrino, 2006), its deployment as part of a morphing structure (Brinkmeyer et al., 2016; Mallol et al., 2017; Mao et al., 2017a; Pedivellano and Pellegrino, 2019), and its viscoelastic constitutive behaviour (Borowski et al., 2018; Khan et al., 2017; Kwok and Pellegrino, 2017;

Mao et al., 2017b). Research on the characterisation of strain levels is however rare, which nevertheless inform the structural integrity of a CTS and ensure that the composite is not over-confined and liable to damage during and after folding.

In order to investigate the implementation of the CTS as a hinge-safety connection within an aircraft landing system, it is essential to understand the ‘‘ploy’’ region, which corresponds to the transitional state between the folded and extended configurations, see Figure 1. We have investigated the CTS shape during folding and its final static shape (Wang et al., 2019a). Folding under equal-sense bending, initiates from torsional buckling, localisation and then steady folding at large displacements (Seffen et al., 2019); the folded tape shape is dominated by axial strains and transverse curvature changes (Wang et al., 2019b). A remaining issue is the strain distributions within the ploy region.

In terms of strain measurements for composite structures, conventional techniques relay on extensometers, strain gauges, as well as digital image correlation (DIC) technique. Extensometer can be applied through surface attachments or contactless using laser tracking system (reflection bands are essential), while it tracks deflections only in the loading plane, and its accuracy suffers from imperfect attachments to the measured surfaces. The DIC is a simple and easy implementing optical non-destructive testing (NDT) technique, providing more accurate strain monitoring than extensometers and strain gauges (Pan, 2018). Although it offers 3D strain mapping capability, the DIC technique is susceptible to highly dynamic and multidimensional analysis, the aeras of interest need to be exposed to the CCD camera throughout the measuring, which significantly constrains its applications to structural testing and evaluations (Wang et al., 2020b). Folding nature of CTS is highly dynamic, and contains large deflections in all three dimensions (Wang et al., 2019b), where, both extensometer and DIC are hardly to be employed to give effective full-range strain data. As for strain gauge, although it provides limited precision and tracks strain changes only at a single point, it offers advantages in terms of cost-effectiveness and flexibility, which in turn providing opportunities to track the full-range structural deflections through designate experimental design. Therefore, strain gauges are applied to study the folded strains of the CTS structure.

In this research, we develop a novel method to evaluate the strain evolution in a folded CTS. The strain along a tape is measured by using embedded strain gauges. A CTS is rolled

through at a constant folding angle of 160˚. Thus the measured strains represent the entire strain range along the folded tape. An FE model is then established and verified through experiments. Further insight therefore can be drawn from the 3D strain mapping from the FE model. The paper is organised as follows. Section 2 introduces theoretical analysis of the shape of a folded CTS. Section 3 describes the characterisation methods through experiments and finite element (FE) simulation. Section 4 presents the results, and Section 5 gives the discussion on folded ploy strains. Section 6 concludes the study.

2 Folded tape shape

For a CTS folded under pure end moments, its shape has three clear regions: the circular fold itself (radius of *r*), Region-A, which connects to the start of the ploy region Region-B over which the change in transverse curvature, χ_y, decays before the undeformed straight end Region-C (radius of *R*) (Wang et al., 2019b), see Figure 1. A simple estimation of the circular fold radius is: $r = \sqrt{D_{11}/D_{22}}\,R$, thus for our woven composite, $r = R$, which is similar to an isotropic tape-spring (Calladine, 1988a). Although it is noted there is slight difference in between (Seffen, 2001) which can be solved by counting the boundary layer effects (Calladine and Seffen, 2020). At the connection between regions A and B, axial curvature, $\kappa_x = 1/r$, and transverse curvature, $\kappa_y = 0$, which define the theoretical boundaries of the ploy region. One solution for this shape is given by (Seffen et al., 2019):

$$\chi_x = -\frac{k^2}{R} e^{-k\frac{\pi x}{b}} \left[1 - \cos\left(\frac{\pi y}{b}\right)\right] \tag{1}$$

$$\chi_y = -\frac{1}{R} e^{-k\frac{\pi x}{b}} \cos\left(\frac{\pi y}{b}\right) \tag{2}$$

$$\chi_{xy} = \frac{k}{R} e^{-k\frac{\pi x}{b}} \sin\left(\frac{\pi y}{b}\right) \tag{3}$$

where *k* is a decay parameter, defined as:

$$k^4 = \frac{B}{36S} \frac{\beta}{1 - v^2/\beta} \frac{t^2 R^2}{b^4} \tag{4}$$

where b is tape width, t is thickness, and β is modular ratio defined as $\beta = E_y/E_x$. This allows the ploy region length, L^*, to be estimated:

$$L^* = \frac{b^2}{\pi}\left[\frac{1-v^2/\beta}{120\beta}\right]^{1/4}\sqrt{\frac{c}{t}} \tag{5}$$

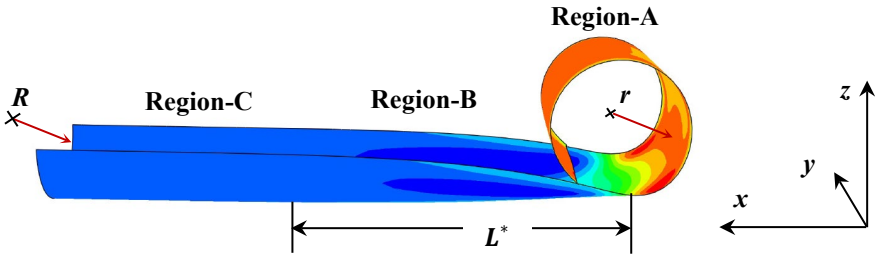

Figure 1 **Shape of a folded composite tape-spring: the circular fold itself (radius of *r*), Region-A, connects to the start of the ploy region Region-B (with characteristic length, L^*), and undeformed straight end Region-C (radius of *R*).**

For equal-sense bending, the axial strain, ε_{11}, varies linearly through thickness, where outer surface is under tension (+), and inner surface in compression (−) (Yee and Pellegrino, 2005), it is maximised by the longitudinal curvature changes, χ_x, and follow:

$$\varepsilon_{11} = \pm\, \chi_x\, t/2 \tag{6}$$

3 Folded strain characterisations

3.1 Experimental

Strain evolution in a folded CTS is measured through quasi-static rolling of a CTS with embedded strain gauges along a folded angle of 160°. Thus the measured strains represent the entire strain range along the folded CTS. The CTS sample is typically 200 mm long, with a radius of 13 mm and subtended 180˚. The strain gauges are from Tokyo Sokki Kenkyujo Co. Ltd., with 6 mm width, 120 Ω resistance, a thermal expansion coefficient of 11 μm/(m·˚C), and transverse sensitivity (K_t) of 0.1%.

Table 1 **Material properties of GF fabrics (MatWeb Materials Information Database, 2017a) and PP sheets (MatWeb Materials Information Database, 2017b).**

Materials	GF fabric	PP sheet	
Density	200 g/m^2	0.9 g/cm^3	0.9 g/cm^3
Thickness (mm)	0.20	0.5	0.05
Construction warp×weft (th/cm)	7.4×7.4	--	--
Type of yarn	EC9 68×2	--	--
Poisson's ratio	0.2	0.42	
Elastic modulus (GPa)	72.4	1.53	
Shear modulus (GPa)	30	0.54	
Thermal expansion coefficient (μm/m°C)	5.0	84.8	

In order to produce a CTS sample, plain-weave glass fibres (GFs) and polypropylene (PP) sheets were used and followed previous procedures (Wang et al., 2020a), their properties are shown in Table 1. Strain gauges were embedded in the composite layup to ensure direct contact and good bonding with constituents. For repeatability, three strain gauges were embedded along the central line 50 mm (SG-01), 100 mm (SG-02) and 150 mm (SG-03) away from the tip, see Figure 2. After heat treatment, each strain gauge was carefully connected to a National Instrument PXIe-1071 series transducer. The CTS sample was then clamped at the bottom end; the top end was pre-bent to 90˚ to facilitate rolling, and attached to an Instron 4483 machine with a 30 kN load cell at room temperature. Strain data were measured by displacing the crosshead at 60 mm/min with a data acquisition rate of 2 Hz.

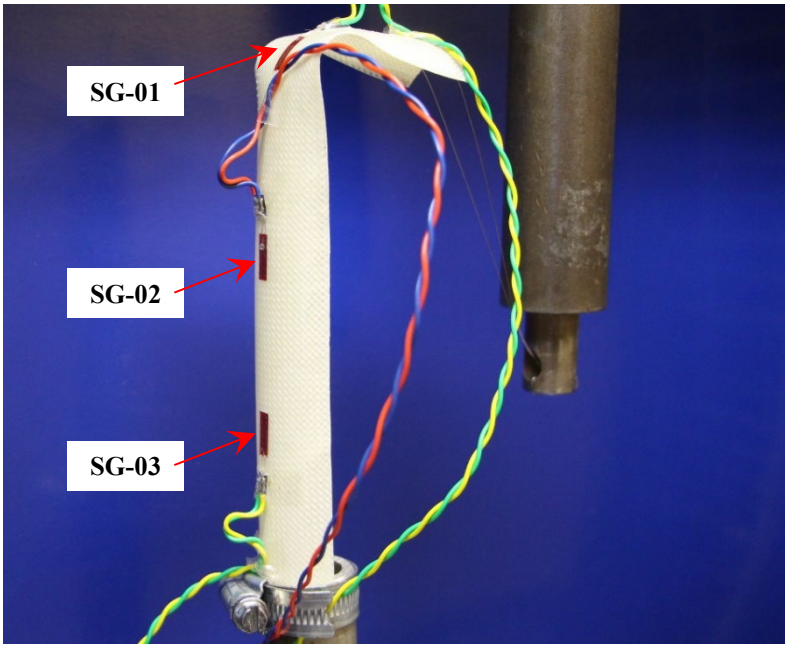

Figure 2 **Experimental setup for measuring the strain in the ploy region.**

A Leica DM LM optical microscope was then used to evaluate the cross-section of the composite sample. The depth of the embedded strain gauge was measured from the micro-images using an open accessed software FIJI (Schindelin et al., 2012), in order to assess the position of the measured strains.

3.2 Finite element model

The FE model followed the previously described model (Wang et al., 2019b) using ABAQUS/Explicit (Abaqus User Manual, 2014). For woven composite materials, we used an approximation following Naik's model (Naik and Ganesh, 1995), which provides a close approximation of the membrane stiffness (Akkerman, 2006; Mallol et al., 2017). To match the experimental setup in Figure 2, the FE model used the following sequences to apply load and boundary conditions:

Step-01: one end of the tape is constrained in all directions, and the other is flattened;

Step-02: the flattened end of the tape is pre-bent to 90˚;

Step-03: the bent end is displaced along a line inclined at 20˚ to the vertical direction.

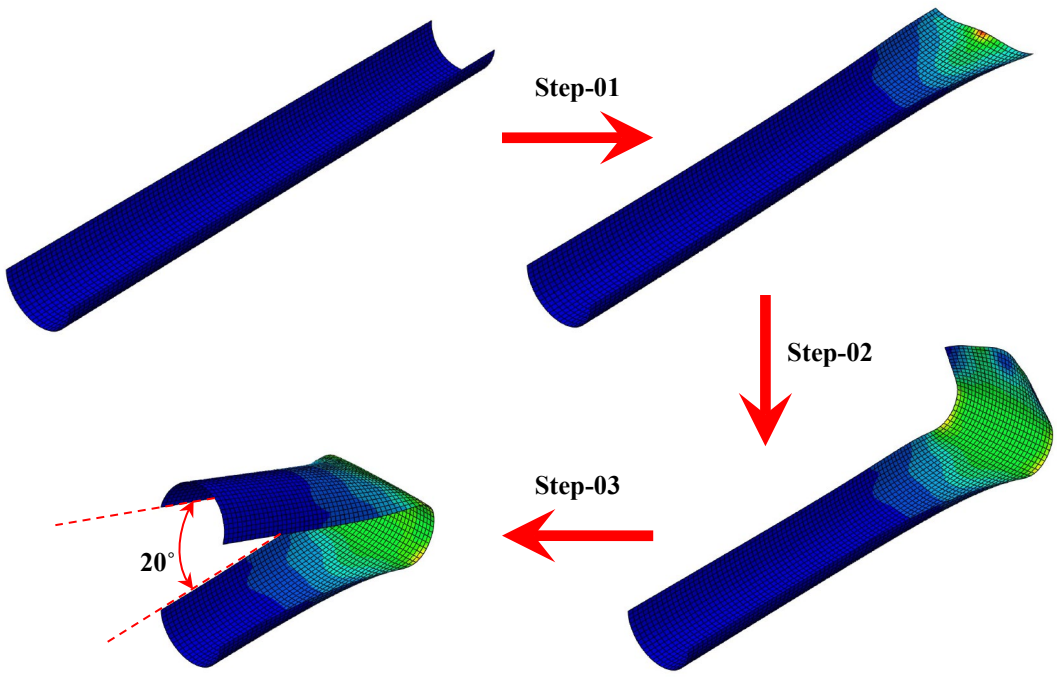

Figure 3 **Finite element model to map strains in rolling of a CTS, colour shows the stress counter.**

The shell model used S4R elements, with a damping factor of 1×10^{-6} during solution. An element size of 2 mm and around 2000 elements in total were adopted, as in (Wang et al., 2019b). Steps 1 and 2 are applied to match the experimental constraints, see Figure 3, and strain data from Step-3 are analysed with those from experiments.

4 Results

4.1 Strains along a tape

Figure 4 shows the strain and load profiles by rolling a CTS sample. The CTS end is pre-bent, which gives an initial strain reading of 0.012 from SG-01; 0.001 for SG-02 (which is marginal); and SG-03 is barely affected, since the ploy length for this tape is 54 mm as predicted by Eqn 5. The load is comparatively steady through the rolling process, with a value of 5 ± 2 N, which increases quickly as it approaches the fixed tape end. The undulations in loads are caused by periodic ‘‘kinks’’ in the central fold region, see the inset in Figure 4. It also affects the shape of the strain curves, *e.g.* the peak in strain curve is rounder from SG-01 than SG-02. This is further supported by the FE analysis and discussed later.

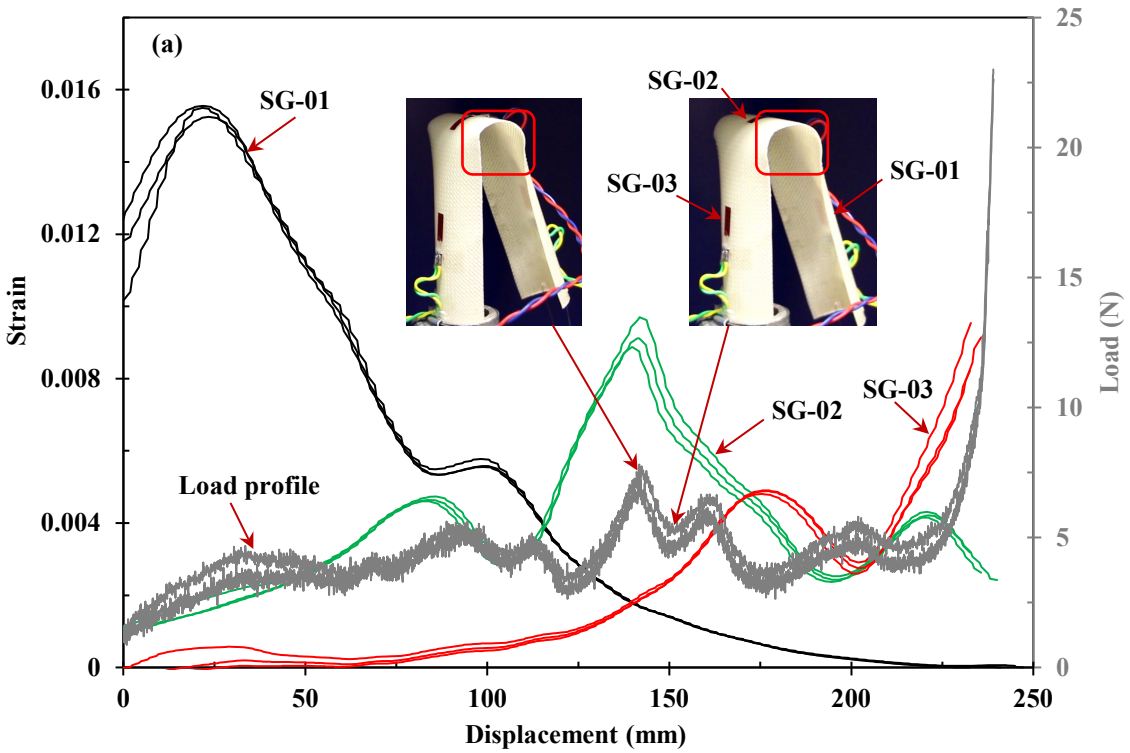

Figure 4 Experimentally measured axial strain and load profiles by rolling a CTS sample with three embedded strain gauges.

The rolling shape provides an exact profile of the strain everywhere along the CTS centreline once the fold reaches the bottom end. The maximum strain is found at the centre of the folded tape as expected. One interesting feature beyond the fold, is the "shoulder-like" local peak as observed in all three strain gauges.

4.2 Verification of the FE model

The depth of the strain gauge was assured from the sample surface to the mid-thickness, results are shown in Table 2, and they were found to be located at 28%, 35% and 33% of thickness for SG-01, SG-02 and SG-03, respectively. These enable direct comparisons of strain evolutions to the FE model, which assumes a linear strain variation through the thickness according to Kirchoff's hypothesis (Calladine, 1988b).

Table 2 **Depth of the strain gauges as measured from the cross sectional images, and SR is the ''standard error''.**

	Depth (mm) ± SR	Sample thickness (mm) ± SR
SG-01	0.204 ± 0.006	0.743 ± 0.007
SG-02	0.264 ± 0.006	0.741 ± 0.011
SG-03	0.241 ± 0.008	0.723 ± 0.006

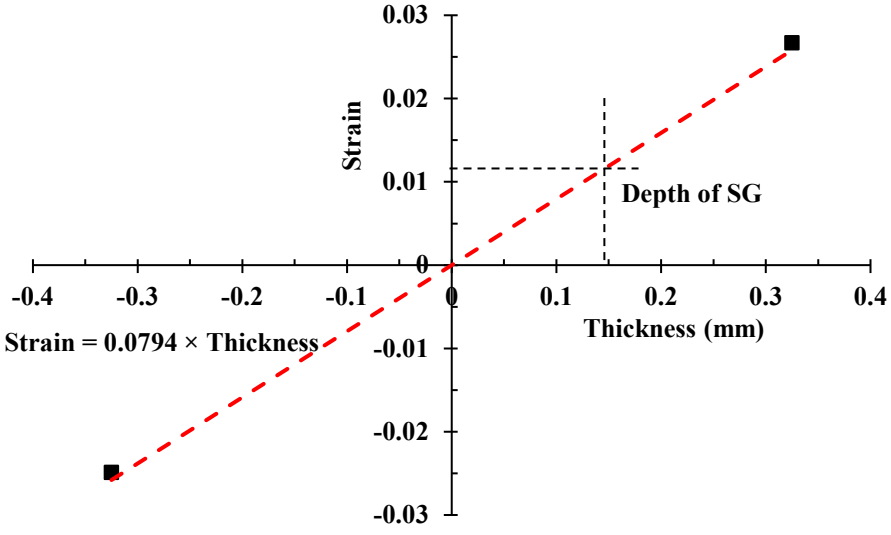

Figure 5 **Axial strain change along thickness direction from the FE model, considering the mid-plane to be symmetric. Black squares are data points extracted from the model; red dashed line shows the strain prediction through thickness direction; black dashed lines present the real depth of the embedded strain gauge (SG) given in Table 2.**

Figure 5 shows the longitudinal strain change along thickness direction, considering the mid-plane to be symmetric. Positive strain is under tension and correlates to the outer surface of the tape, whereas negative strain shows compressive behaviour on the inner surface. The gradient of the linear fit is thus the curvature change (χ_x) of the mid-plane.

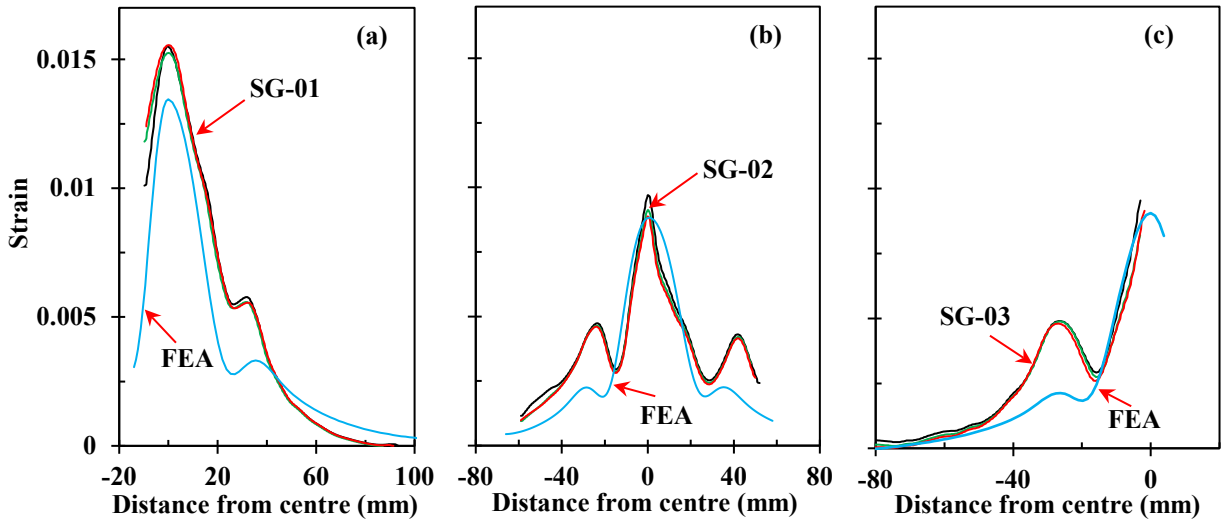

Figure 6 **Comparison of the axial strain changes from experiments and FE model. FE data are extracted from the same depth of the strain gauges given in Table 2. The central peak corresponds to the centroid of the CTS.**

Figure 6 now compares the strain data from experiments and the FE model, with the distance from the fold centre. The FE predictions broadly show the same trends from all three positions; but there are some discrepancies in strain values. These variations may result from the effect locally of embedding strain gauges, which adds additional thickness to the sample and causes non-uniform local distribution of matrix material. The differences may also be attributed to strain values being measured on the average of the covered areas (13.2 mm^2), while the FE strains are from a single node point. Strain data at the peaks and valleys in Figure 6 are extracted and shown in Table 3. The FE model provides close predictions of the central peak strain, giving a mean underestimation of around 8%. The model also provides a reasonable prediction of the position of the ‘‘shoulder’’ feature.

Table 3 **Strain data at peaks and valleys extracted from Figure 6, showing the mean values ± standard errors. For SG-02, the ‘‘shoulder’’ feature is captured twice, thus there are two groups of data denoted separately as ‘‘left side’’ and ‘‘right side’’ with respect to the fold centre.**

	Central peak strain (%)	Shoulder valley		Shoulder peak	
		Strain (%)	*d* (mm)	Strain (%)	*d* (mm)
SG-01	1.54 ± 0.01	0.54 ± 0.01	26.50 ± 0.27	0.56 ± 0.01	31.85 ± 0.31
FEA	1.35	0.28	27.04	0.33	35.49
Difference	-12%	-48%	2%	-46%	11%
SG-02	Left side	0.29 ± 0.01	-15.03 ± 0.10	0.47 ± 0.01	-23.83 ± 0.31
FEA		0.19 ± 0.01	-20.49	0.22	-29.27
Difference		-34%	-36%	-53%	-23%
	0.92 ± 0.02	--	--	--	--
FEA	0.88	--	--	--	--
Difference	-4%	--	--	--	--
	Right side	0.24 ± 0.01	28.90 ± 0.15	0.42 ± 0.01	41.72
FEA		0.19	27.36	0.23	35.91
Difference		-21%	-5%	-45%	-14%
SG-03		0.28 ± 0.01	-15.87 ± 0.02	0.49 ± 0.01	-26.37 ± 0.27
FEA		0.18	-19.71	0.21	-26.28
Difference		-36%	-24%	-57%	-0.3%

5 Discussion

We know that a folded tape shape consists of three regions. The theoretical regional shape boundaries can be identified by plotting out the transverse curvature changes (χ_y) along the central line of the CTS from the FE model (Wang et al., 2019a). Thus, the boundaries defined as ‘‘MNTPQ’’ are applied to Figure 6 (a), and reproduced in Figure 7. The exponential decay is fitted by Eqn 2 with $k = 0.62$. These boundaries are essential for understanding the strain distribution through the folded tape.

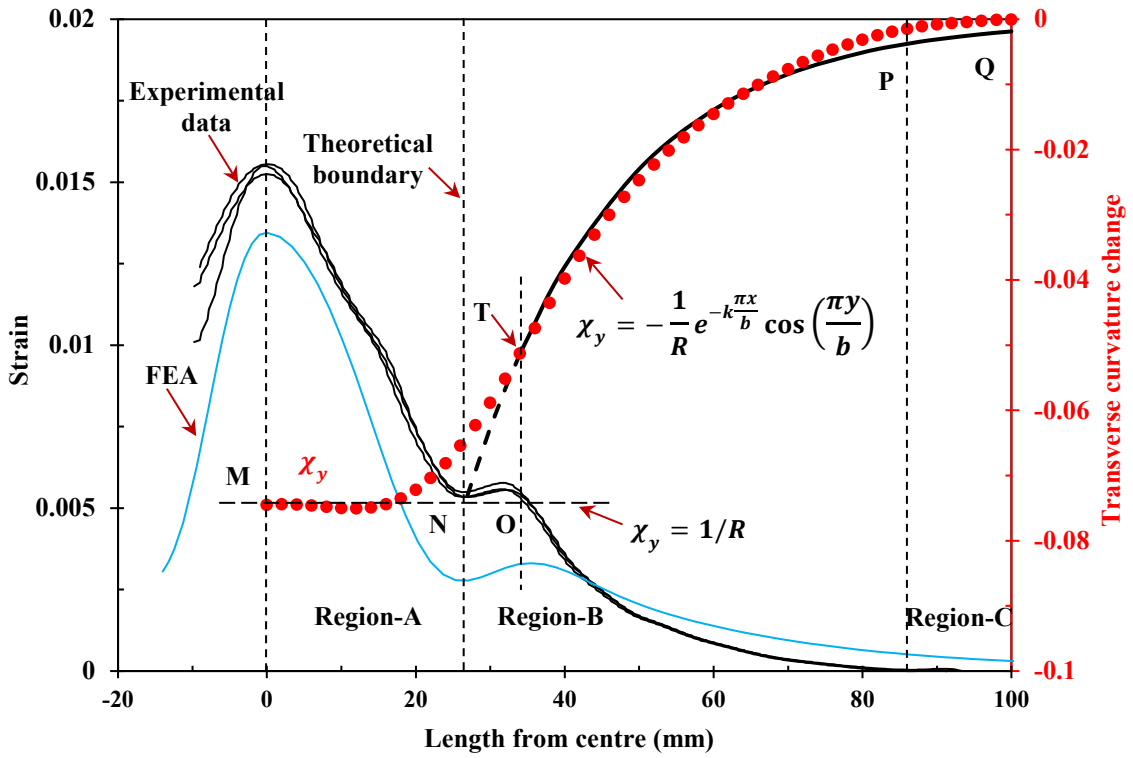

Figure 7 **Folded tape strain measured from both experiments and FE simulation. The circular data points present the transverse curvature changes (χ_y) along the central nodes of a folded CTS from the FE model; the curve is fitted by Eqn 2, and the dotted curve is its extension. The theoretical boundaries of folded CTS shape are defined by ''MNTPQ''.**

The central fold Region-A undergoes the maximum axial strains as expected. Away from the centre, there is an almost linear drop in strain values up to the ploy Region-B, where the shoulder feature appears. It is worth noting that the valley of the shoulder corresponds to the theoretical boundaries between Region-A and Region-B, denoted as point ''N'' in Figure 7; the shoulder peak correlates to point ''T'', which is a transition point, defined as onset of exponential decay in χ_y. It is also noted that there is a constant underestimation of strain values out from the fold centre to around 44 mm away. Experimental strains are then lower than the FE model. These effects may be due to the viscoelastic response of the real tape sample, whilst viscoelasticity is not implemented in the FE model. Thus, the ploy Region-B can be characterised by a peak strain feature, which extends our knowledge on the ploy region of a folded tape-spring.

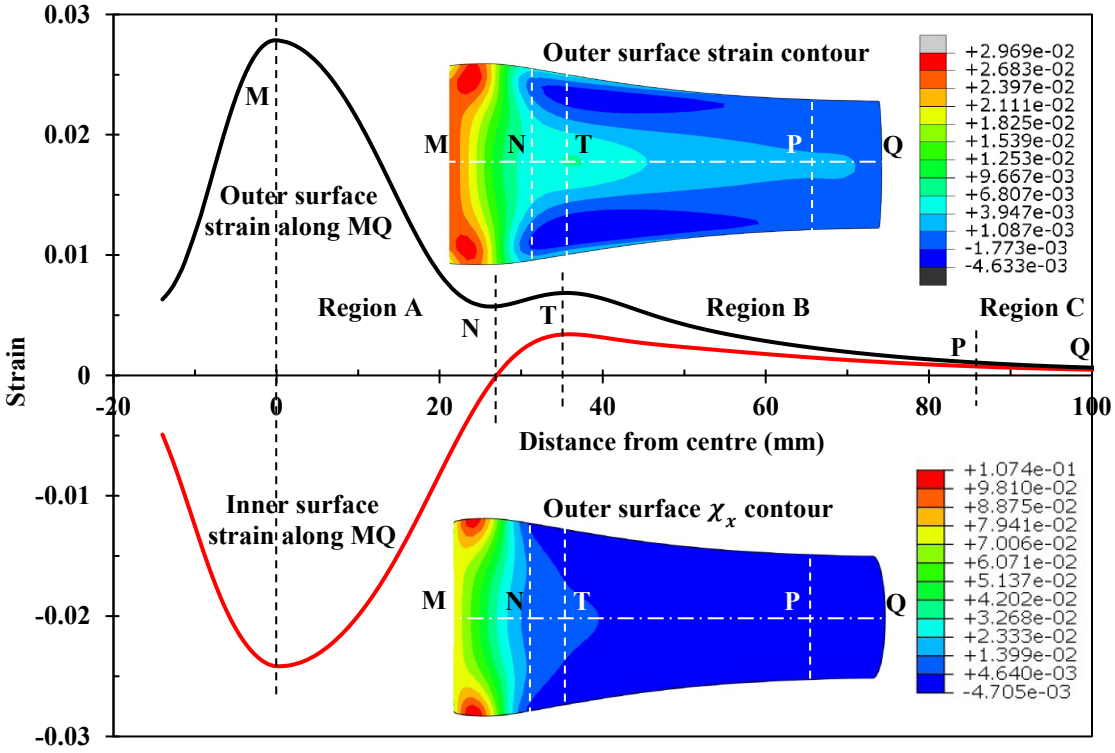

Figure 8 **Surface strain profiles from the FE model, the inset show the strain contour (top) and χ_x contour (bottom) of the outer surface. Boundaries denoted by ''MNTPQ'' are in line with Figure 7.**

Therefore, further insight can be drawn from the FE model. Figure 8 shows the surface strain profiles along the fold centre line (MQ), and the defined boundaries, MNTPQ, from Figure 7 are superposed. Along MQ, both axial tensile and compressive strains are maximised at the fold centre Region-A as indicated by Eqn 6. It is also noted from the inset strain contours that higher strains occur in both tension and compression near the sides of the fold centre Region-A, which correspond to the areas with maximised χ_x as highlighted by the inset. These strain concentration regions are most likely to develop into the ''kinks'' as observed experimentally and highlighted in Figure 4. Away from the fold centre, both the tensile and compressive strains dissipate. At point N, the compressive strain changes sign on the inner surface, and reaches maximum tensile strain at the transition point T.

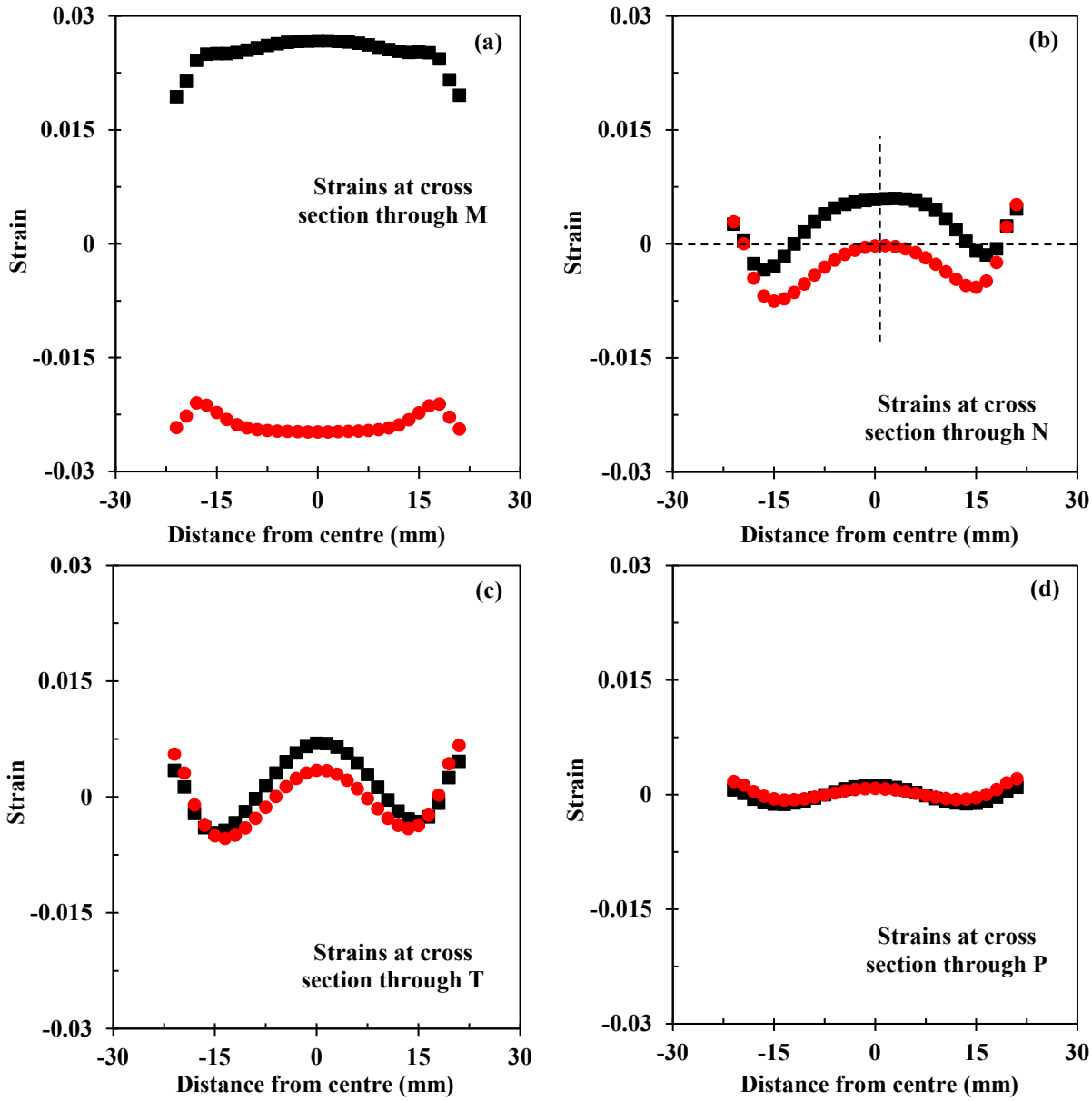

Figure 9 **Longitudinal surface strain values on the cross-sections of the tape at the boundaries denoted as M, N, T, and P. Black squares are outer surface strains, and red dots show inner surface strains.**

The surface strain values across the transverse section of the tape at the boundaries are plotted against the tape width, see Figure 9. Positive values again are tensile and negative values give a compressive response. In the centre of the fold, the strain is almost uniform across the width, see Figure 9-a. At the cross-section through N, the inner surface strain is effectively zero, with tension and compression across the surfaces, Figure 9-b. Beyond the transition point, strains on both surfaces become approximately the same, see Figure 9-c and d.

6 Conclusions

We devise a novel method to evaluate experimentally the strain evolution within a folded CTS. An FE model is established and verified through experimental data, which indicates further insight.

The shape of a folded tape consists of three regions: the circular central fold Region-A; ploy Region-B; and natural end Region-C. The ploy region has a natural length scale of minimal deformation which is dependent on the initial tape geometry. The ploy shape is dominated by axial strains and transverse curvature changes. There are two peak strain features along a folded tape: (i) the strains are maximised at the central fold region; (ii) an additional ‘‘shoulder’’ feature is also observed in the ploy region. The shoulder valley corresponds to the theoretical boundaries between Region-A and Region-B, where the compressive strain changes sign on the inner surface of the CTS. Whilst the shoulder peak correlates to the transition point ‘‘T’’, where tensile strain on the inner surface is maximised. These findings extend the knowledge on ploy strain distributions within a CTS, and facilitate designs to maintain structural integrity of the tapes as in a load-bearing safety hinge assembly, in order to ensure the composite is not over-confined and liable to damage during and after folding.

CRediT authorship contribution statement

Bing Wang: Investigation, Data curation, Software, Formal analysis, Writing – original draft, Project administration. Keith A Seffen: Supervision, Validation, Writing – review & editing, Funding acquisition. Simon D Guest: Supervision, Validation, Writing – review & editing, Funding acquisition.

Declaration of interests

The authors declare that they have no known competing financial interests or personal relationships that could have appeared to influence the work reported in this paper.

Acknowledgements

The authors would like to acknowledge the financial supports from Innovate UK on project ‘‘Large Landing Gear of the Future: Bistable Composite Technologies’’ (Grant No. 113077, RG82506), in close partnership with SAFRAN Landing Systems Ltd., UK. B.W. thanks the support from National Natural Science Foundation of China (52005108). We also thank the technical staff and aegis of the National Research Facility for Infrastructure Sensing (NRFIS, Grant No. EP/P013848/1), Cambridge University Engineering Department.

References

Abaqus User Manual, 2014. Abaqus theory guide. Version 6.14. Dassault Syst. Simulia Corp.

Akkerman, R., 2006. Laminate mechanics for balanced woven fabrics. Compos. Part B Eng. 37, 108–116.

Borowski, E.C., Soliman, E.M., Khan, A.I., Taha, M.M.R., 2018. Stowage and deployment of a viscoelastic orthotropic carbon-fiber composite tape spring. J. Spacecr. and Rockets 55, 829–840.

Brinkmeyer, A., Pellegrino, S., Weaver, P.M., 2016. Effects of long-term stowage on the deployment of bistable tape springs. J. Appl. Mech. 83, 11008.

Calladine, C.R., 1988a. The theory of thin shell structures 1888–1988. Proc. Inst. Mech. Eng. Part A Power Process Eng. 202, 141–149.

Calladine, C.R., 1988b. Theory of Shell Structures. Cambridge University Press, Cambridge.

Calladine, C.R., Seffen, K.A., 2020. Folding the Carpenter’s tape: Boundary layer effects. J. Appl. Mech. 87, 011009.

Galletly, D.A., Guest, S.D., 2004a. Bistable composite slit tubes. I. A beam model. Int. J. Solids Struct. 41, 4517–4533.

Galletly, D.A., Guest, S.D., 2004b. Bistable composite slit tubes. II. A shell model. Int. J. Solids Struct. 41, 4503–4516.

Guest, S.D., Pellegrino, S., 2006. Analytical models for bistable cylindrical shells. Proc. R. Soc. A Math. Phys. Eng. Sci. 462, 839–854.

Khan, A.I., Borowski, E.C., Soliman, E.M., Taha, M.M.R., 2017. Examining energy dissipation of deployable aerospace composites using matrix viscoelasticity. J. Aerosp. Eng. 30, 4017040.

Kwok, K., Pellegrino, S., 2017. Micromechanics models for viscoelastic plain-weave composite tape springs. AIAA J. 55, 309–321.

Mallol, P., Mao, H., Tibert, G., 2017. Experiments and simulations of the deployment of a bistable composite boom. J. Spacecr. Rockets 1–11.

Mao, H., Luigi, G.P., Michele, G., Nickolay, I., Gunnar, T., 2017a. Deployment of bistable self-deployable tape spring booms using a gravity offloading system. J. Aerosp. Eng. 30, 4017007.

Mao, H., Shipsha, A., Tibert, G., 2017b. Design and analysis of laminates for self-deployment of viscoelastic bistable tape springs after long-term stowage. J. Appl. Mech. 84, 71004–71010.

MatWeb Materials Information Database, 2017a. E-Glass Fiber, General. URL http://www.matweb.com/search/datasheet.aspx?MatGUID=d9c18047c49147a2a7c0b0bb1743e812&ckck=1 (accessed 11.13.17).

MatWeb Materials Information Database, 2017b. Overview of materials for polypropylene. URL http://www.matweb.com/search/DataSheet.aspx?MatGUID=1202140c34e8443bbf273862e24c5f0e (accessed 11.15.17).

Naik, N.K., Ganesh, V.K., 1995. An analytical method for plain weave fabric composites. Composites 26, 281–289.

Pan, B., 2018. Digital image correlation for surface deformation measurement: historical developments, recent advances and future goals. Meas. Sci. Technol. 29, 82001.

Pedivellano, A., Pellegrino, S., 2019. Stability analysis of coiled tape springs, in: AIAA Scitech 2019 Forum. p. 1523.

Schindelin, J., Arganda-Carreras, I., Frise, E., Kaynig, V., Longair, M., Pietzsch, T., Preibisch, S., Rueden, C., Saalfeld, S., Schmid, B., Tinevez, J.-Y., White, D.J., Hartenstein, V., Eliceiri, K., Tomancak, P., Cardona, A., 2012. Fiji: an open-source platform for biological-image analysis. Nat. Methods 9, 676.

Schmidt, R.K., 2017. Aircraft landing gear assembly. EP3069991B1.

Seffen, K.A., 2001. On the Behavior of Folded Tape-Springs. J. Appl. Mech. 68, 369–375.

Seffen, K.A., Wang, B., Guest, S.D., 2019. Folded orthotropic tape-springs. J. Mech. Phys. Solids 123, 138–148.

Wang, B., Seffen, K.A., Guest, S.D., 2019a. Shape of a bistable composite tape-spring in folding, in: AIAA SciTech 2019 Forum. San Diego, pp. 1–12.

Wang, B., Seffen, K.A., Guest, S.D., 2019b. Folding of bistable composite tape-springs. University of Cambridge, Department of Engineering.

Wang, B., Seffen, K.A., Guest, S.D., Lee, T.-L., Huang, S., Luo, S., Mi, J., 2020a. *In-situ* multiscale shear failure of a bistable composite tape-spring. Compos. Sci. Techno. 200, 108348.

Wang, B., Zhong, S., Lee, T.-L., Fancey, K.S., Mi, J., 2020b. Non-destructive testing and evaluation of composite materials/structures: A state-of-the-art review. Adv. Mech. Eng. 12, 1–28.

Yee, J.C., Pellegrino, S., 2005. Composite tube hinges. J. Aerosp. Eng. 18, 224–231.